Revision 2

Word count: 9482

X-ray absorption records of Pd^{2+} on Ni site in pentlandite

Valeriya Brovchenko*[1], Margarita Merkulova[2], Jonathan Sittner[2], Vladimir Shilovskih[3], Camelia Borca[4], Thomas Huthwelker[4], Sergey F. Sluzhenikin[1], Veerle Cnudde[2,5]

[1]Institute of Geology of Ore Deposits Mineralogy, Petrography, and Geochemistry, Russian Academy of Sciences, Staromonetny per. 35, Moscow 119017, Russia

[2]PProGRess-UGCT, Geology Department, Ghent University, Krijgslaan 281, Ghent 9000, Belgium

[3]Centre for Geo-Environmental Research and Modeling, St. Petersburg State University, Ulyanovskaya ul. 1, St. Petersburg 198504, Russia

[4]Swiss Light Source, Paul Scherrer Institute, Villigen PSI 5232, Switzerland

[5]Department of Earth Sciences, Utrecht University, Princetonlaan 8a, Utrecht 3584, The Netherlands

*valeriiabrovchenko@gmail.com

Abstract

Norilsk sulfide ores are one of the largest known sources of Pd on Earth. Palladium in these ores is presented in platinum-group minerals (PGM) and base metal sulfides (BMS), especially in pentlandite ($(Fe,Ni)_9S_8$). Although several studies demonstrated high concentrations

along with heterogeneous distribution of Pd in pentlandites from Norilsk, the form of Pd in pentlandite has not been established. Here, we provide the first evidence for Pd incorporation in the lattice of pentlandite from Norilsk ores. These results were obtained by combining X-ray absorption near edge structure (XANES) spectroscopy, synchrotron-based micro-X-ray fluorescence (μXRF), and electron backscatter diffraction (EBSD). We present the first ever measured XANES spectra of Pd in pentlandite and atokite ($(Pd,Pt)_3Sn$) as well as in other common Pd minerals. Divalent Pd in pentlandite was detected by XANES. The Pd spectra in pentlandite show no similarities with Pd spectra in PGM, metallic Pd, PdS, $PdCl_2$, and $PdSO_4$ which signifies that Pd incorporates into the lattice of pentlandite. Substitution of Ni by Pd in the lattice of pentlandite is supported by negative correlations shown by μXRF and electron probe microanalysis (EPMA) and complies with the previous studies. The additional EBSD study demonstrates a resemblance in cell parameters of the Pd-rich and Pd-poor parts of the pentlandite grains and reflects that Pd incorporation into the pentlandite structure does not imply any notable structure distortion. The combination of analytical techniques used in the present study demonstrates the great potential of these methods for understanding the mechanisms of noble metal incorporation into ore minerals.

Keywords: Palladium, pentlandite, platinum-group minerals, XANES, μXRF, EBSD, EPMA

Introduction

Palladium, like other platinum-group elements (PGE), occurs as discrete platinum group minerals (PGM) or in base metal sulfides (BMS), associated with mafic intrusions (Godel et al., 2007; Barnes et al., 2008) and komatiite flows (Keays et al., 1981; Lesher and Keays, 2002). Pentlandite (Pn) among other base metal sulfides appears to be a principal host in most deposits.

The highest concentration of Pd in Pn (up to 11.26 wt%; Kalugin et al., 2021) was reported from the Southern 2 orebody of the Talnakh deposit (Russia). The origin of Pd in Pn is debated. Kalugin et al. (2021) attributed the high Pd concentrations in Talnakh pentlandite to the influence of Pd-rich fluids. The Pd-rich pentlandite from the J-M reef ores, Stillwater deposit (Montana) contains up to 9.8 wt% of Pd, which is believed to be a secondary enrichment during the hydrothermal redistribution of Pd from the surrounding PGM (Li and Ripley, 2006). Until recently, most works assumed based on experimental work (Kelly and Vaughan, 1983; Etschmann et al., 2004; Helmy et al., 2021), that pentlandite formed by exsolutions from monosulfide solid solution (MSS) in the non-altered magmatic sulfide ores. However, the partition coefficient of Pd into MSS is <0.2, thus the presence of bulk Pd in pentlandite requires an explanation (Barnes et al., 1997; Liu and Brenan, 2015). Makovicky et al., 1986 showed that Pd solubility in MSS increases with temperature. Upon cooling, MSS rejects Pd and transforms into pyrrhotite, and pentlandite, the latter can incorporate Pd. Some authors suggested that PGE are present in silicate liquid as clusters (Tredoux et al., 1995; Helmy et al., 2020), and these clusters were captured by the sulfide liquid and incorporated into the MSS. Pre-nucleation clusters of Ir, Os, Ru, and Rh are present as metal-metal, metal-S, and metal-AsS complexes, but Pt and Pd form semimetal (As, Te, Bi, Sb) complexes (Helmy et al., 2013; Laurenz et al., 2013; Helmy and Bragagni, 2017; Liang et al., 2022). The experimental work of Kitakaze et al. (2016) offers an alternative namely that of pentlandite having formed by peritectic reaction at high temperature between monosulfide solid solution (MSS) and a residual sulfide liquid. An example of this is the granular Pn that occurs at the contact between pyrrhotite (Po) and chalcopyrite (Cpy) and tends to be enriched in Pd at the contact with Cpy compared to the Pn in contact with Po (Dare et al., 2010; Mansur et al., 2019; Brovchenko et al., 2020). In this case, it is argued that Pd preferentially partitions into Pn and thus should be a part of the lattice structure. According to

Makovicky et al. (2016) pentlandite dissolves up to 5.4 at.% of Pd and 92 % of Pd occupy the octahedral site in the lattice. Based on correlations between Pd content and Ni/Fe ratio in zonal Pd-rich Pn, Kalugin et al. (2021) concluded the isomorphic substitution of Ni by 0.71 apfu Pd and 0.3 apfu Fe. Wirth et al. (2013) and Junge et al. (2015) used focused ion beam (FIB) combined with transmission electron microscopy (TEM) to study the site of Pd in Pn from the Merensky and UG-2 reefs of the Bushveld Complex (South Africa). Wirth et al. (2013) found Pd to be present as nanonuggets (of Pd-Sn and Pt-Pd-Sn compounds) in Pn and Junge et al. (2015) found Pd to be present both as part of the Pn lattice and as nanonuggets. The question arises as to whether the nanonuggets represent clusters and are an important part of the budget of Pd. Some authors argue that nanonuggets are essential to the formation of PGE deposits (Tredoux et al., 1995; Helmy et al., 2013; Anenburg and Mavrogenes, 2020; Kamenetsky and Zelenski, 2020). On the other hand, those working with laser-ablation inductively coupled plasma mass spectrometry (LA-ICP-MS) argue that for time-resolved analysis signals (TRA) each time slice represents ~0.2 to 0.6 microns of material ablated and a constant signal shows that the element uniformly present in the mineral on this scale (Page and Barnes, 2016) implying that the element (in this case Pd) is in solid solution in the mineral (Pn).

The Norilsk-Talnakh deposits of Siberia (Russia) are one of the largest known sources of Pd in the world (Naldrett, 2011; Barnes et al., 2020). The distribution of Pd in pentlandite from various Norilsk-Talnakh ore deposits has been studied by a number of analytical methods, including electron probe microanalysis (EPMA), LA-ICP-MS, and particle-induced X-ray emission (PIXE) (Cabri et al., 1984; Czamanske et al., 1992; Distler et al., 1996; Cabri et al., 2003; Barnes et al., 2006; Mansur et al., 2019; Brovchenko et al., 2020; Kalugin et al., 2021). These studies provided valuable information on the concentration and distribution of Pd in

pentlandite. Brovchenko et al. (2020) showed that primary magmatic pentlandite in massive ores of Mt. Rudnaya offshoots, Norilsk-Talnakh deposits, contains a high concentration of Pd (up to 4.62 wt%). A comprehensive geological review of the Mt. Rudnaya offshoots is presented in Brovchenko et al. (2020). The deepest terminations of the Mt. Rudnaya ores had a specific globular texture composed of Cu-rich intermediate solid solution (ISS) globules up to 4 mm in size surrounded by MSS-ISS fine-grained matrix with MSS outward bands between matrix and globules. Both MSS and ISS are relatively high-temperature sulfides that are transformed to BMS at subsolidus temperatures (Craig and Kullerud, 1969; Cabri, 1973). Therefore, the presence of MSS and ISS in natural sulfide ores indicates that these ores formed due to the fast quenching of a primary magmatic sulfide melt (Helmy et al., 2021). The most enriched in Pd and the biggest pentlandite grains (with a size up to 100 μm) are predominately confined to the contact between ISS globules and MSS outward bands. Moreover, Pd in these pentlandite grains is heterogeneously distributed with an increase of concentration from the contact with MSS toward the contact with ISS. Such type of enrichment of contact pentlandite was considered to display its peritectic reactional origin (Brovchenko et al., 2020). The current work focuses on Pd incorporation in Mt. Rudnaya pentlandite.

X-ray absorption spectroscopy (XAS), which includes X-ray absorption near-edge structure (XANES) and extended X-ray absorption fine structure (EXAFS), can be used to determine the local structure of elements in minerals. These techniques have been successfully applied to reveal chemical state and atomic position of Au in Fe-sulfides (Tagirov et al., 2016; Trigub et al., 2017; Merkulova et al., 2019; Pokrovski et al., 2019), Hg in pyrite and marcasite (Manceau et al. 2018), Pt in synthetic pyrite (Filimonova et al., 2019), As and Se in pyrite (Manceau et al., 2020) and Pt in pyrrhotite (Filimonova et al., 2021). To the best of our

knowledge, no attempts have been made to use XAS to detect the speciation and occurrence of Pd in pentlandite. The main limitation could be the low concentration of Pd in natural pentlandite, difficulties in the experimental synthesis of homogenous Pd-doped pentlandite, and lack of familiarity of geoscientists with this technique combined with its difficult accessibility. Thus, besides evidence of the form of Pd in pentlandite from the Bushveld complex, the site of Pd in pentlandite from other major PGE ore deposits is still unconfirmed.

In the present study, we report the oxidation state and structural form of Pd in pentlandite from the Norilsk ore deposit by using XANES in combination with synchrotron-based micro-X-ray fluorescence (μXRF) and electron backscatter diffraction (EBSD). Additionally, we determine the oxidation state of Pd in metallic Pd, PdS, $PdCl_2$, $PdSO_4$, and in six different PGM to compare XANES spectra of Pd in pentlandite and other common Pd-bearing compounds. This work is the first to show Pd L_3-edge XANES measurements in pentlandite and PGM. The EBSD showed the granular structure of the sample and did not demonstrate any deformations inside the crystallites of Pd-rich pentlandite. The outcome of this study provides new insights into the substitutional mechanism of Pd in pentlandite and encourages further use of XAS methods in mineralogy and ore geology.

Materials and Methods

Sulfide mineral samples were collected from the deepest terminations of Mt. Rudnaya subvertical massive sulfide offshoots in the NE of the Norilsk 1 deposit (Brovchenko et al., 2020). Twenty polished blocks were examined using a petrographic light microscope, a scanning electron microscope (SEM), XRF, EPMA, LA-ICP-MS, and X-ray computed micro-tomography (micro-CT) prior to this study. The descriptions of these samples, analytical methods and the results of the analyses are described in detail in Brovchenko et al. (2020) and Sittner et al. (2022).

Apart from BMS, Mt. Rudnaya MSS-ISS ores also contain PGM up to 125 μm in size such as tetraferroplatinum (PtFe), Pt-Fe alloys having the compositions Pt_2Fe and Pt_3Fe_2, cooperite (PtS), Pd- rich rustenburgite (Pt_3Sn), Pt-rich atokite (Pd_3Sn), and Au-Ag alloys, mostly occurring in the ISS globules (Sittner et al., 2022). Three sample blocks, namely RM 10, RM 29, and RM 30, containing pentlandite with the highest concentration of Pd (up to 4.84 wt%), were selected for the current study. Pentlandite grains in these selected samples occur at the contact with Cu-rich ISS globules and Cu-poor MSS outward bands, surrounded by MSS-ISS fine-grained matrix as described in Brovchenko et al. (2020). Additionally, six different Pd-bearing PGM were selected from the Mineralogical Collections of the Technische Universität Bergakademie Freiberg (Germany) for the XANES and μXRF measurements. The origin and composition of the investigated minerals are listed in Table 1.

The sulfide mineral samples from Norilsk and PGM grains were mounted in epoxy and polished. The epoxy mounts were polished with 3-to-1 μm diamond suspension before every analytical procedure, including synchrotron measurements. This was done to remove the oxidized layer that can form on the surface of sulfide minerals and PGM. Synchrotron-based XANES and μXRF measurements were acquired on beamline PHOENIX I at the Swiss Light Source (SLS, Switzerland). Measurements were performed in fluorescence-yield mode and with a focused beam for Norilsk samples and PGM grains. Concentrated powders of Pd compounds (PdS, $PdCl_2$, $PdSO_4$), used as references for XANES, were measured with an unfocused beam in electron-yield mode. The electron-yield mode was used to exclude self-absorption effects that occur in fluorescence XAS for concentrated samples.

The incoming X-ray beam was monochromatized by the 111 reflection of a Si double crystal monochromator. The flux on the sample was approximately 5×10^{10} photons s^{-1}. The size

This is the peer-reviewed, final accepted version for American Mineralogist, published by the Mineralogical Society of America.
The published version is subject to change. Cite as Authors (Year) Title. American Mineralogist, in press.
DOI: https://doi.org/10.2138/am-2022-8704. http://www.minsocam.org/

of the unfocused beam was 1×1 mm^2. The beam focused with a set of Kirkpatrick-Baez (K-B) mirrors had a size of 4×4 μm^2. The fluorescence intensity was measured with a Si drift detector (4 element Vortex, Hitachi, USA). The samples were positioned at 45° with the respect to the incident X-ray beam and the detector. All measurements took place under vacuum at 1×10^{-6} mbar.

Elemental μXRF maps were obtained by scanning the sample with an incident focused beam with an energy of 3174 eV, and a dwell time of 1 s. Single-point μXRF spectra were collected with a beam energy of 3174 eV and a collection time of 300s. All XRF data were analyzed using PyMCA software (Sole et al., 2007).

The spots with the high Pd signal on the μXRF maps also called "hot spots" were selected for the XANES analysis. The incident energy for the Pd L_3-edge XANES spectra was scanned from 3100 to 3327 eV for all samples and references. The XANES spectra could not be evaluated over a larger energy range due to the presence of the Pd L_2-edge at 3330 eV. The spectra were recorded with a step of 5 eV for the pre-edge region (3100-3165 eV), 0.3 eV for the edge and XANES region (3166-3190 eV), and with a step increasing from 1 to 2.4 eV for the post-edge region (3191-3327 eV). One XANES spectrum per measurement was taken for Pd references, 1-3 spectra per sample were taken for PGM grains, and from 1 to 41 spectra per point measurement were taken for pentlandite. No beam damage was observed during repeated scans on the same point of a sample. The XANES spectrum of a Pd foil was measured 1-2 times every 24 hours during the beamtime in order to follow an energy shift of the incident beam. No energy shift was observed. The absolute energy of the spectra is referenced to the maximum of the Pd^0 (Pd foil) derivative taken to 3173.8 eV. The precision of the energy measurement is ± 0.1 eV. The XANES spectra of all PGM grains including a PGM grain from Norilsk samples were corrected

for the self-absorption effect. The relative energies between spectra were established by a careful comparison of the first derivatives. The XANES spectra were reduced, normalized and corrected for self-absorption with the Athena software (Ravel and Newville, 2005).

Concentrations of the major and trace elements in pentlandite were determined by an JEOL JXA 8200 EPMA at the "IGEM-Analitika" analytical centre. The EPMA is equipped with five wave-length spectrometers. Measurements were operated at 20 kV accelerating voltage, 20 nA beam current per Faraday cylinder, and 1 μm beam diameter. The counting time for Fe (Kα, LIF), S (Kα, PET), Ni (Kα, LIF), Cu (Kα, LIF), and Co (Kα, LIF) was 10 s for the peak and 5 s for the backgrounds. Natural $CuFeS_2$ was used as a reference for Cu, Fe, and S determination; and NiSbS was utilized for analyzing Ni and Co. Pure synthetic Pd was used as reference materials for Pd (Lα, PET) determination with 20 s counting time for the peak and 10 s for the backgrounds. Pure native Pt was used as a reference material for Pt (Lα, LIF) determination at 60 s counting time for the peak and 30 s for the backgrounds. Native Ag was used as a reference material for Ag (Lβ, PET) determination at 30 s counting time for the peak and 15 s for the backgrounds. Synthetic GaAs was used for As (Lα, TAP) determination with a counting time of 30 s for the peak and 15 s for the backgrounds. The analytical conditions provided detection limits (3 standard errors) of around (wt %) 0.08 for Cu, 0.07 for Pt, 0.06 for Co, 0.05 for As, 0.04 for Ag, and 0.02 for Pd. The uncertainty of the concentrations was estimated from the reproducibility of home standard analysis as <5 % rel. (2 standard errors).

Homogeneity and distribution of crystallographic orientations within the above-mentioned Pd-rich pentlandite grains were studied with EBSD using Hitachi S-3400 SEM equipped with Oxford NordLysNano EBSD detector and Oxford X-max 20 energy-dispersive X-Ray analyzer (EDX) ("Geomodel" resource center, St Petersburg University (SPbU)).

Acquisition conditions were as follows: 30 kV accelerating voltage, 5 nA beam current, step size 0.5-1 μm, averaging of 3 patterns per point. All the patterns were processed automatically using Oxford AztecHKL software, the maps were created with the Channel5 software. The reference structure for pentlandite was taken from Inorganic Crystal Structure Database (ICSD, number 61021). Prior to EBSD studies, Ar ion polishing was performed (Oxford IonFab 300, 10 min exposure, 500 V accelerating voltage, 200 mA beam current, at "Nanophotonics" resource center, SPbU) to remove the mechanically deformed layer from the surface.

Results and Discussion

Distribution of Pd and element correlations

Elemental mapping by synchrotron-based μXRF was employed to investigate the distribution of Pd and its correlations with other elements, notably Ni, Cu, S, and Pt. The μXRF mapping shows a heterogeneous distribution of Pd in sulfides. Figure 1a provides the elemental distribution maps of Pd, Ni, Cu and S analyzed on sample RM 30_3. The association of Pd with Ni shown on the elemental map documents that Pd is localized only in pentlandite and not in the Cu-rich intermediate sulfide solid solution (ISS) or Fe-rich MSS. The Pd hot spot in the sample has a size of 45×30 μm^2 and is the biggest among detected Pd-rich areas in all samples. Two Pd-rich spots (2×3 μm^2) to the left and bottom of the main Pd-rich region in pentlandite might represent Pd-bearing PGM. However, due to the small size, it was not possible to measure a XANES or μXRF spectrum at these locations. Similar elemental correlations and the same elemental distribution are observed on elemental maps of samples RM 29_1 and RM 29_3 (Supplementary Figures S2, S3, and S4). No Pt fluorescence was observed in the scanned areas. Four Pd-rich domains in the three sulfide mineral samples are related to pentlandite. In contrast, one Pd-rich region was found in sample RM 10_3, which has other elemental correlations (Figure

229 1b). The Pd in sample RM 10_3 correlates positively with Pt. No Ni or Cu are detected in the Pd-
230 rich zone. The detected Pd hot spot represents a Pd-bearing PGM grain with a size of 10×6 μm^2.

231 Micro-XRF spectra recorded in the hot spots of Pd are presented in Figure 2. Four μXRF
232 spectra taken in Pd hot spots of samples RM 29 and RM 30 are very similar to each other and
233 indicate the occurrence of Pd in pentlandite, which in turn was determined based on the
234 occurrence of the Ni peak at 0.848 keV (Figure 2a). Figure 2b shows μXRF spectra of pentlandite
235 from sample area RM 30_3, a PGM grain from sample RM 10_3, and pentlandite and ISS matrix
236 in sample RM 29_1. The four spectra are evidently different. The μXRF spectra in the matrix of
237 pentlandite and ISS were recorded to demonstrate that no intense Pd Lα peak (2.838 keV) is
238 observed in the matrix material. A low intensity noisy peak at the energies of Pd Lα is observed
239 in the spectra and attributed to the entrance of Pd fluorescence from the Pd hot spot in the
240 proximity of the matrix area. Therefore, the Pd fluorescence in all μXRF spectra is attributed to
241 the Pd-rich pentlandite and PGM. Platinum, identified by the high-intensity Mα peak at 2.047
242 keV is clearly visible in the spectrum of PGM grain. Whereas no Pt peak is observed in the
243 spectrum of pentlandite and matrix regions. Other peaks that can be identified in the μXRF
244 spectra are Fe (Lα = 0.704 keV), S (Kα = 2.309 keV), Cu (Lα = 0.928 keV), Si (Kα = 1.740
245 keV), Al (Kα = 2.309 keV). Iron and sulfur are major elements in both, pentlandite and ISS
246 matrix, and they are often detected in different Pd-bearing PGM (e.g., Sluzhenikin et al., 2020).
247 Copper is a major element in ISS. The appearance of fluorescence peaks of Si and Al in the
248 spectrum of the sample RM 30_3 is explained by the presence of small holes common for the
249 samples and containing Si- and Al-bearing debris from polishing. In the case of sample RM 30_3
250 the holes are located near the Pd hotspot and are therefore recorded in the μXRF measurements.

The above observations based on μXRF measurements confirm the occurrence of Pd in at least two forms in the studied samples from Norilsk. Palladium within pentlandite grains and Pd within the PGM grain. The relationship between Pd and Ni in pentlandite determined by μXRF was additionally examined by EPMA. The Pd concentrations of up to 4.84 wt.% were detected. Quantitative EPMA measurements (Table S1) indicated a negative correlation between the two elements with a Pearson correlation coefficient of -0.97. In addition, EPMA analyses demonstrated a positive correlation between Pd and Fe with a Pearson correlation coefficient of 0.65 (Figure 3).

EBSD study of the Pd-rich pentlandite grains

Diffraction contrast maps show that the pentlandite crystallites exhibit the same quality over the entire grain surface and thus the existence of nanocrystalline Pd inclusions is improbable (Figure 4). Grain boundaries divaricate to the Pd-rich and Pd-poor zones contact (Figures 4e, 4f, and 4g) and do not correlate with Pd content (Figure 4c), nor any defect accumulation is observed between Pd-rich and Pd-poor zones. The orientation maps correspond to a polycrystalline growth from a common border. The patterns acquired in the areas with different Pd content within the same crystallite do not differ in either the bands positions or bandwidth. The resemblance between the patterns suggests that the presence of Pd in the structure does not lead to a noticeable distortion of the structure of pentlandite (Figures 4a and 4b), which means Ni is substituted by Pd in the structure. The additional EBSD data are presented in the Supplementary material (Figures S6 and S7).

Oxidation state of Pd in PGM

The Pd L_3-edge XANES spectra of the six PGM and the Pd metal reference are shown in Figures 5a and 5b. The six spectra of the PGM grains differ from each other, which is consistent with the different atomic coordination of Pd in these six minerals. The PGM spectra are shifted to higher energy relative to Pd foil (metallic Pd^0). The energy positions of the white lines, feature marked as a', of the PGM and the reference spectra are listed in Table 2. The energy positions of the white lines for the PGM spectra vary from 3174.7 eV for vasilite to 3175.6 eV for paolovite. The difference in white line energy for the vasilite and paolovite spectra compared to the white line of metallic Pd is 0.9 and 1.8 eV respectively. The PGM spectra are shifted towards higher energies compared to the spectrum of metallic Pd demonstrating a higher oxidation state of Pd in the PGM grains. The energy positions of the white lines are 3174.4 eV for $PdCl_2$, 3174.7 eV for $PdSO_4$, and 3175.3 eV for PdS. These energies are in the same range as the energies of the PGM. This indicates that Pd in the studied PGM grains has an oxidation state of +2. An oxidation state of +4 for Pd is excluded since the energy position for Pd^{4+} compounds is expected to be at much higher energies, 3176.8 eV for Zn_2PdO_4 (Kim et al., 2002), 3184.6 eV for $[PdCl6]^{2-}$ (Barton, 2013), 3188.3 eV, $[N_4PdCl_2]^{2+}$ (Barton, 2013). The difference in energy between the measured spectra varies from 3174.4 eV for $PdCl_2$ to 3175.6 eV for paolovite. This can be interpreted as an electronegativity effect of neighboring ligands. The white line of the $PdCl_2$ spectrum has the lowest energy due to the high electronegativity of Cl (3.16) compared to other ligand atoms (electronegativity of S = 2.58; Bi = 2.02; As = 2.18; Sn = 1.96; Ni 1.91; Cu = 1.9). The higher the electronegativity of a ligand atom, the lower the energy position of the white line.

The XANES spectrum of the PGM grain from sample RM 10_3 is shown together with the spectra of the PGM named above in Figure 5a and with the Pd references in Figure 5b. The energy position of the RM 10_3 PGM spectrum is 3175.1 eV, almost identical to that of atokite.

Moreover, the second spectral feature, indicated as b' in Figure 5a, of the RM 10_3 PGM coincides with that of atokite. Based on the presence of the intense Pt peak on the μXRF spectrum for the RM 10_3 PGM grain and the resemblance of its XANES spectrum to the spectrum of atokite, we propose that the PGM in sample RM 10_3 can be identified as atokite. Atokite is a common Pd-bearing mineral and is often described in sulfide mineral assemblages of Norilsk ores (Barkov et al., 2000; Sluzhenikin et al., 2020), including Mt. Rudnaya MSS-ISS ores (Brovchenko et al., 2020). Nanometer-sized atokite has also been identified as one of the most favored forms of Pd occurrence in pentlandite (Junge et al., 2015). Thus, the detection of atokite in our samples is valuable for the comparison of various possible forms of Pd in minerals.

Oxidation state and bonding of Pd in pentlandite

The four Pd hot spots in pentlandite depicted on μXRF maps (Figure 1 and Supplementary material) were selected for Pd L_3-edge XANES measurements. The XANES spectra in these four pentlandite grains from four different sample areas are identical (Figure S8 in Supplementary material), suggesting that there is only one form of Pd identified in the Mt. Rudnaya pentlandite. The Pd hot spot in sample RM 30_3 is the biggest among the detected Pd-rich pentlandite grains. Forty-one spectra were collected on the same position of this Pd hot spot and averaged to get a spectrum with better statistics. The obtained averaged spectrum is plotted together with XANES spectra of PGM and Pd references in Figures 5a and 5b. The position of the white line of the pentlandite spectrum is in the range of energies for all measured PGM and Pd references, based on that this energy position is assigned to Pd^{2+}. The white line of the pentlandite coincides with the energy of the white line of vasilite. This match can be explained by the bonding of palladium with sulfur in the two sulfide minerals, pentlandite, and vasilite. The position of the white line of the PdS reference is 0.3 eV higher than that of pentlandite. Such a

difference could be explained by the fact that a "mixed electronegativity" is present in pentlandite due to the different elements (Fe, Ni, and S) involved in the bonding compared to the exclusive "pure" bonding of Pd and S in PdS.

Figures 5a and 5b demonstrate that the white line of the pentlandite spectrum is more intense compared to those of PGM, metallic Pd, and PdS. The interpretation of white line intensities is challenging because several effects can influence the white line intensities of the L_3-edge XANES. Given small uncertainty due to the normalization of the spectra and correction of the PGM spectra to self-absorption, these effects can be due to nanoparticle size, adsorbate effect, and alloying effect (Koningsberger et al., 2000; Zheng et al., 2011; Todorovic, 2012). We exclude the contributions of size and adsorbate effect since they are not relevant to our samples. It is known that the intensity of the white line of L_3-edges in XANES for 4d metals is correlated with the number of unoccupied d states (Muller et al., 1982; Sham, 1985). In pure metals and their alloys, d states are full and the white line is less pronounced (Sham, 1985). Alloying of Pd with other metals that can be present in the minerals and compounds showed here results in changes to the electronic structure of Pd, in particular occupancy of the d state, and consequently decreases the intensity of the white line (Sham, 1985; Kim et al., 2002; Witjens et al., 2004). The high intensity of the L_3-edge white line of the pentlandite spectrum thus can be explained by the absence of alloying of Pd in the mineral. In contrast, lower white line intensities of the PGM spectra demonstrate a possible alloying of Pd with other metals in the mineral structures. Indeed, the PGM studied here contain metals (Pt, Cu, Ni) or metalloids (Sn, Te, Bi) that form short bonding distances with Pd (Mihalik et al., 1975; Matkovic et al., 1976; Bayliss et al., 1990; Evstigneeva et al., 2000) contributing to the alloying of Pd.

The shape of XANES spectra is usually indicative of the atomic configuration. The different shape of the pentlandite spectrum compared to PGM and Pd references, therefore, confirms that Pd in pentlandite does not occur in micro-inclusions of the present Pd compounds, but has its own atomic coordination.

Pd substitution in pentlandite

The μ-XRF and XANES results of this study confirm the existence of two forms of Pd in the Mt. Rudnaya MSS-ISS ores, Pd associated with PGM inclusions and Pd incorporated in pentlandite. XANES analysis demonstrates that palladium in pentlandite and PGM is represented by Pd^{2+}. Following the presented results, we conclude that Pd related to pentlandite is incorporated into the structure of the mineral. This is the first report of Pd incorporation in the lattice of pentlandite from Norilsk, which is based on direct spectroscopic measurements. Considering the positive charge of Pd, we propose that Pd occupies a cationic position in the pentlandite structure. Iron and nickel in the pentlandite crystal structure evenly occupy octahedral and tetrahedral sites (Rajamani and Prewitt, 1975). As noted by Junge et al. (2015), the electronic configuration of Pd is similar to that of Ni (dsp^2) and not to Fe, which can be an argument for the preferential occupation of Ni sites by Pd. Kalugin et al. (2021) also noted a preferable substitution of Ni sites by Pd. And although ionic radii of Pd^{2+} for tetrahedral (0.64 Å) and octahedral (0.86 Å) coordination is closer to ionic radii of Fe^{2+} (0.64 Å, 0.78 Å) than to those of Ni^{2+} (0.55 Å, 0.69Å) (Shannon, 1976), our findings of the negative correlation between Pd and Ni and positive correlation between Pd and Fe in pentlandite suggests that palladium prefers to be substituted on the place of Ni. A resemblance of the ionic radii of Pd, Ni, and Fe accounts for an absence of any structure distortion of pentlandite noticed on EBSD orientation maps. Whereas, in contrast, Ag addition into pentlandite (argento pentlandite $(Fe_5Ni_3)AgS_8$; Mandziuk and Scott,

1977) causes distortion of the pentlandite structure due to the difference of the ionic radius between Ag (1.15 Å for Ag^{1+} in an octahedral configuration) and the substituted Fe and Ni (Shishkin, 1972). The silver ionic radius is almost twice as much as Pd, while another isomorphic component, typical for pentlandite, is Co which has a similar ionic radius (0.58 Å, 0.74 Å) to Pd. It has been demonstrated that Co incorporation into pentlandite leads to a decrease in the cell size (Riley, 1977) and growth of temperature range for pentlandite stability (Vaasjoki et al., 1974). Riley (1977) showed that Co substitutes either Fe and Ni making two different series with octahedral or tetrahedral Co atoms coordination in pentlandite structure. In the pentlandites form the MSS-ISS ores of Mt. Rudnaya, Co (as from 0.29 to 0.53 wt%) negatively correlates with the Fe/Ni ratio displaying Co accommodation mostly in the Fe site with a Pearson correlation coefficient between Fe and Co in aphu of -0.4 (Table S1). Co and Pd contents in pentlandite from J-M reef ores, Stillwater deposit, correlate positively (Godel and Barnes, 2008), although these components do not correlate with each other in Pd-rich pentlandite from Talnakh deposit (Kalugin et al. 2021). The Pearson correlation coefficient for Co and Pd in pentlandite from Mt. Rudnaya MSS-ISS ores (in apfu) is -0.45 (Table S1), which can be described by the additional substitution of Co by a minor part of Pd atoms in the Fe site.

Origin of Pd-rich pentlandite

As mentioned above, Pd-rich pentlandite can be formed in two ways. One way is exsolution from MSS below 450 °C (Etschmann et al., 2004, Helmy et al., 2021). Concentration of Pd dissolved in MSS at 900 °C can reach 11 wt. %. Upon cooling, Pd solubility in MSS decreases, and its concentration drops to 0.4 wt. % at 500 °C (Makovicky et al., 1986). Contact pentlandite starts to grow at 450 °C as the flame-like nano exsolutions from MSS (Helmy et al., 2021). Pd partitions into these exsolutions formed at the rims of MSS grains by diffusion.

Whereas the diffusion rate of pentlandite in MSS shows its maximum at 400 °C and drops below this temperature (Etschmann et al., 2004). The second scenario for Pd-rich pentlandite formation involves a peritectic reaction between Ni-poor MSS and Ni-rich residual sulfide melt at 870-800 °C, followed by eutectic reaction directly from the melt at ~750 °C (Kitakaze et al., 2016). Although literature data on Pd solubility in high-temperature pentlandite is not available, it is reported that pentlandite associated with Pd-rich phases contains up to 4 at.% of Pd at 550 °C in the Pd-Ni-Fe-S phase system (Makovicky and Karup-Møller, 2016). Pd partitions into peritectic pentlandite from residual sulfide melt which is far more enriched in Pd than MSS. This causes directional enrichment trends in the pentlandite grains: from ISS, more compatible with Pd, to MSS, less compatible with Pd (Liu and Brenan, 2015; Mansur et al., 2019).

When both types of pentlandite are present, exsolved Pd-poor pentlandite can equilibrate with early-formed peritectic Pd-rich pentlandite at a grain boundary, resulting in gradual trends of Pd enrichment in one grain (Barnes S.-J. et al., 2020). The crystallographic orientation of the subsolidus pentlandite can be inherited from early-formed peritectic pentlandite. Pd-rich zones in pentlandite from Mt. Rudnaya MSS-ISS ores are confined to either rims or central parts of grains. Pd-rich pentlandite appears as 10-100 μm loop-like and coarse grains at the contact between MSS and ISS, and as up to 50 μm disseminated euhedral grains in ISS. Pd-rich zones in disseminated pentlandite are surrounded by ISS and present only in the central parts of grains. In contrast, Pd-rich zones in pentlandite from the contact between MSS and ISS (studied in this work) are confined to the contact with ISS or the inner parts of grains, with a maximum also located closer to ISS. In the scenario of pentlandite exsolution from MSS, the most enriched in Pd zones must be at the edges of grains and disappear gradually towards the contact with MSS, because Pd, as a non-coherent element, rather enriches the rims of MSS than random parts. Pentlandite which is

409 later formed by exsolution must feed on the broken MSS at the MSS-ISS boundaries and have the
410 same trends of enrichment. However, the majority of Pd-rich zones are found in the inner parts of
411 pentlandite grains. More probably, this type of Pd enrichment indicates the peritectic origin of
412 Pd-rich pentlandite when both MSS and sulfide liquid can be the feeding environments, and the
413 directional distribution of other trace and major elements confirms this (Brovchenko et al., 2020).
414 The disseminated pentlandite grains among ISS had an eutectic origin. However, formation of
415 Pd-rich pentlandite exsolved from MSS was also probable and we can suggest that this
416 pentlandite could be formed after the peritectic pentlandite. As a result, these Pd-poor pentlandite
417 exsolutions equilibrated with the peritectic Pd-rich pentlandite, setting the directional trend of Pd
418 enrichment.

419 **Implications**

420 For the first time, Pd L_3-edge XANES has been measured in natural Pd-rich pentlandite
421 and various natural PGM. The combined μXRF and XANES results demonstrate that Pd
422 incorporates in the crystal structure of pentlandite. By comparing XANES data for Pd in
423 pentlandite and various natural PGM and synthetic Pd, PdS, $PdCl_2$, and $PdSO_4$ we exhibit a
424 difference between Pd spectra in these common Pd-bearing phases.

425 The form of Pd in pentlandite and the formation of Pd-rich pentlandite from PGE ore
426 deposits are still debated. Nano and micro-inclusions of various PGM were described in different
427 sulfide minerals (Wirth et al., 2013), including pentlandite (Junge et al., 2015). Junge et al.
428 (2015) also demonstrated the presence of Pd solid solutions in the lattice of pentlandite from the
429 Bushveld complex. However, the contents of Pd in pentlandite from Junge et al. (2015) are on
430 average 390 ppm. High concentrations of Pd in Pn from the Talnakh deposit (Kalugin et al.,
431 2021) and J-M Reef (Li and Ripley, 2006) were achieved by the hydrothermal secondary

redistribution leading to additional incorporation of Pd predominantly in the Ni site (Kalugin et al., 2021). Here, we show the first evidence of incorporation of Pd in pentlandite from the non-altered Mt. Rudnaya MSS-ISS ores as up to 4.84 wt%. Our findings leave no doubt about the possibility of Pd entering the crystal structure of pentlandite as a solid solution. The coexistence of primary magmatic high-temperature sulfide phases such as MSS, ISS, and pentlandite with a high Pd content as well as the exceptionally high bulk PGE content in ores (up to 350 ppm), support the idea of the primary magmatic origin of ores from the fractionated residual Cu-Ni-PGE enriched sulfide liquid described in Brovchenko et al. (2020). The rapid quenching, therefore, ensured the preservation of high-temperature MSS and ISS, and the heterogeneous distribution of trace and major elements. Also, the recent X-ray microtomography study by Sittner et al., (2022) declares a specific globular three-dimensional texture of these ores. It seems to be supportive of an idea of a possible sulfide-sulfide liquid immiscibility between Cu-richer and Cu-poorer liquids in the exceptionally Cu and Ni enriched sulfide systems. The most enriched in Pd grains of pentlandite (studied in the current work) are confined to these globular textures, namely at the contact between Cu-richer ISS globules and Cu-poorer MSS-ISS fine-grained matrix. The fact that palladium could be incorporated into the structure of pentlandite with such high concentrations in not-altered primary magmatic ores can potentially reveal that the solubility of Pd in pentlandite extends with temperature and encourages the determination of new constraints on the physical-chemical conditions of ore-forming processes. The ability of BMS to dissolve PGE at high temperatures has also been demonstrated for MSS and Pt (Makovicky et al., 1986; Majzlan et al., 2002), for MSS and Pd (Ballhaus and Ulmer, 1995) and pyrrhotite and Pt (Filimonova et al., 2021). Our data confirm the possibility of Pd solubility in pentlandite. Therefore, PGE could be concentrated in BMS as solid solutions indicating that the behavior of

455 these elements is preliminary controlled by sulfide melt. It signifies that the role of PGM
456 nanonuggets in the formation of Cu-Ni-PGE deposits has been overestimated.

457 Our results illustrate that the combination of μXRF, XANES, and EBSD provides
458 complementary and full information on the occurrence of Pd in pentlandite. Such combined
459 investigations have great potential in understanding the mechanisms of other noble metals
460 incorporation in ore minerals.

461 **Acknowledgments**

462 This research is a part of the up scaling project “Resource Characterization: from 2D to
463 3D microscopy” and has received funding from the European Institute of Innovation and
464 Technology (EIT). This body of the European Union receives support from the European Union's
465 Horizon 2020 research and innovation program. The backscattered electron diffraction studies
466 were conducted in the Geomodel Resource Center of Saint Petersburg State University and we
467 thank Maxim Lozhkin for the sample’s preparations. The study at IGEM RAS is supported by the
468 Russian Science Foundation (grant 21-17-00119) whereas earlier research was supported by the
469 Russian Foundation for Basic Research (grant 18-05-70073). We are deeply appreciative of the
470 efforts of Axel D. Renno to improve this paper. We thank E.V. Kovalchuk for help with EPMA.
471 We also thank Michael Gäbelein and Andreas Massanek for providing the inventoried samples of
472 platinum-group minerals from the Mineralogical Collections of the Geoscientific Collections of
473 the TU Bergakademie Freiberg. The valuable critical comments and suggestions by S.-J. Barnes,
474 H. Helmy, anonymous reviewer, and K. Kiseeva improved the text significantly.

475 **References**

476 Anenburg, M., and Mavrogenes, J.A. (2020) Noble metal nanonugget insolubility in
477 geological sulfide liquids. Geology, 48(9), 939-943.

478 Ballhaus, C., and Ulmer, P. (1995) Platinum-group Elements in the Merensky Reef: II.
479 Experimental Solubilities of Platinum and Palladium in $Fe_{1-x}S$ from 950 to 450°C under
480 Controlled fS_2 and fH_2. Geochimica et Cosmochimica Acta, 59, 4881–4888.

481 Barkov, A.Y., Martin, R.F., Poirier, G., and Yakovlev, Y.N. (2000) The taimyrite-
482 tatyanaite series and zoning in intermetallic compounds of Pt, Pd, Cu, and Sn from Noril'sk,
483 Siberia, Russia. The Canadian Mineralogist, 38, 599–609.

484 Barnes, S.J., Zientek, M.L., and Severson, M.J. (1997) Ni, Cu, Au, and platinum-group
485 element contents of sulphides associated with intraplate magmatism: a synthesis. Canadian
486 Journal of Earth Sciences, 34(4), 337-351.

487 Barnes, S.J., Cox, R.A., and Zientek, M.L. (2006) Platinum-group element, Gold, Silver
488 and Base Metal distribution in compositionally zoned sulfide droplets from the Medvezky Creek
489 Mine, Noril'sk, Russia. Contributions to Mineralogy and Petrology, 152, 187–200.

490 Barnes, S.J., Taranovic V., Schoneveld L.E., Mansur E.T., Vaillant M.Le, Dare S., Staude
491 S., Evans N.J., and Blanks D. (2020) The occurrence and origin of pentlandite-chalcopyrite-
492 pyrrhotite loop textures in magmatic Ni-Cu sulfide ores. Economic Geology, 115(8), 1777-1798.

493 Barnes, S.J., Prichard, H.M., Cox, R.A., Fisher, P.C., and Godel, B. (2008) The location
494 of the chalcophile and siderophile elements in platinum-group element ore deposits (a textural,
495 microbeam and whole rock geochemical study): Implications for the formation of the deposits.
496 Chemical Geology, 248(3-4), 295-317.

Barnes, S.J., Malitch, K.N., and Yudovskaya, M.A. (2020) Introduction to a Special Issue on the Norilsk-Talnakh Ni-Cu-Platinum Group Element Deposits. Economic Geology, 115(6), 1157-1172.

Barton, R.L. (2013) Multi-edge X-ray absorption near-edge spectroscopic analysis of palladium complexes in II, III, IV oxidation states, 118p, Master Thesis, Montana State University, Bozeman.

Bayliss, P. (1990) Revised unit cell dimensions, space group, and chemical formula of some metallic minerals. The Canadian Mineralogist, 28, 751-755.

Brovchenko, V.D., Sluzhenikin, S.F., Kovalchuk, E.V., Kovrigina, S.V., Abramova, V.D., and Yudovskaya, M.A. (2020) Platinum Group Element Enrichment of Natural Quenched Sulfide Solid Solutions, the Norilsk 1 Deposit, Russia. Economic Geology, 115(6), 1343-1361.

Cabri, L.J. (1973) New data on Phase Relations in the Cu-Fe-S System. Economic Geology, 68, 443–454.

Cabri, L.J., Blank, H., El Goresy, A., Laflamme, J.H.G., Nobiling, R., Sizgoric, M.B., and Traxel, K. (1984) Quantitative Trace-Element Analyses of Sulfides From Sudbury and Stillwater By Proton Microprobe. The Canadian Mineralogist, 22, 521–542.

Cabri, L.J., Sylvester, P.J., Tubrett, M.N., Peregoedova, A., and Laflamme, J.H.G. (2003) Comparison of LAM-ICP-MS and micro-PIXE results for palladium and rhodium in selected samples of Noril'sk and Talnakh sulfides. The Canadian Mineralogist, 41, 321–329.

Craig, J.R., and Kullerud, G. (1969) Phase relations in the Cu-Fe-Ni-S system and their application to magmatic ore deposits. Economic Geology Monograph 4, p. 344–358.

Czamanske, G.K., Kunilov, V.E., Zientek, M.L., Cabri, L.J., Likhachev, A.P., Calk, L.C., and Oscarson, R.L. (1992) A proton microprobe study of magmatic sulfide ores from the Noril'sk-Talnakh District, Siberia. The Canadian Mineralogist, 30(2), 249-287.

Dare, S.A.S., Barnes, S.J., and Prichard, H.M. (2010) The distribution of platinum group elements (PGE) and other chalcophile elements among sulfides from the Creighton Ni-Cu-PGE sulfide deposit, Sudbury, Canada, and the origin of palladium in pentlandite. Mineralium Deposita, 45, 765–793.

Distler, V.V., Kulagov, E.A., Sluzhenikin, S.F., and Laputina, I.P. (1996) Quenched sulfide solid solutions in the ores of the Norilsk deposit. Geology of Ore deposits, 38, 41-53.

Etschmann, B., Pring, A., Putnis, A., Grguric, B.A., and Studer, A. (2004) A kinetic study of the exsolution of pentlandite $(Ni,Fe)_9S_8$ from the monosulfide solid solution (Fe,Ni)S. American Mineralogist, 89(1), 39-50.

Evstigneeva, T., Kabalov, Y., and Schneider, J. (2000) Crystal structure of PdNiAs, ordered member of isomorphous series Pd_2As-Ni_2As. Materials Science Forum, 321, 700-705.

Filimonova, O.N., Nickolsky, M.S., Trigub, A.L., Chareev, D.A., Kvashnina, K.O., Kovalchuk, E.V., Vikentyev, I.V., and Tagirov, B.R. (2019) The state of platinum in pyrite studied by X-ray absorption spectroscopy of synthetic crystals. Economic Geology, 114, 1649–1663.

Filimonova, O.N., Trigub, A.L., Nickolsky, M.S., Chareev, D.A., Kvashnina, K.O., Kovalchuk, E.V., Vikentyev, I.V., Reukov, V.L., Tagirov, B.R. (2021) The state of platinum in pyrrhotite: X-ray absorption spectroscopy study and implications for the role of Fe sulfides as platinum carriers. Mineralogical Magazine, 85(6), 846-861.

Godel, B., Barnes, S.J., and Maier, W.D. (2007) Platinum-group elements in sulphide minerals, platinum-group minerals, and whole-rocks of the Merensky Reef (Bushveld Complex, South Africa): implications for the formation of the reef. Journal of Petrology, 48(8), 1569-1604.

Godel, B., and Barnes, S.J. (2008) Platinum-group elements in sulfide minerals and the whole rocks of the JM Reef (Stillwater Complex): Implication for the formation of the reef. Chemical Geology, 248(3-4), 272-294.

Helmy, H.M., and Bragagni, A. (2017) Platinum-group elements fractionation by selective complexing, the Os, Ir, Ru, Rh-arsenide-sulfide systems above 1020° C. Geochimica et Cosmochimica Acta, 216, 169-183.

Helmy, H.M., Ballhaus, C., Fonseca, R.O., Wirth, R., Nagel, T., and Tredoux, M. (2013) Noble metal nanoclusters and nanoparticles precede mineral formation in magmatic sulphide melts. Nature communications, 4(1), 1-7.

Helmy, H.M., Ballhaus, C., Fonseca, R.O., and Leitzke, F.P. (2020) Concentrations of Pt, Pd, S, As, Se and Te in silicate melts at sulfide, arsenide, selenide and telluride saturation: Evidence of PGE complexing in silicate melts? Contributions to Mineralogy and Petrology, 175(7), 1-14.

Helmy, H.M., Botcharnikov R., Ballhaus C., Deutsch-Zemlitskaya A., Wirth R., Schreiber A., Buhre S., and Häger T. (2021) Evolution of magmatic sulfide liquids: how and when base metal sulfides crystallize? Contributions to Mineralogy and Petrology, 176(12), 1-15.

Junge, M., Wirth, R., and Oberthür, T. (2015) Mineralogical siting of platinum-group elements in pentlandite from the Bushveld Complex, South Africa. Mineralium Deposita, 50, 41–54.

562 Kalugin, V., Gusev, V., Tolstykh, N., Lavrenchuk, A., and Nigmatulina, E. (2021) Origin
563 of the Pd-Rich Pentlandite in the Massive Sulfide Ores of the Talnakh Deposit, Norilsk Region,
564 Russia. Minerals, 11(11), 1258.

565 Kamenetsky, V.S., and Zelenski, M. (2020) Origin of noble-metal nuggets in sulfide-
566 saturated arc magmas: A case study of olivine-hosted sulfide melt inclusions from the Tolbachik
567 volcano (Kamchatka, Russia). Geology, 48(6), 620-624.

568 Kelly, D.P., and Vaughan, D.J. (1983) Pyrrhotine-pentlandite ore textures: a mechanistic
569 approach. Mineralogical Magazine, 47(345), 453-463.

570 Keays, R.R., Ross, J.R., and Woolrich, P. (1981) Precious metals in volcanic peridotite-
571 associated nickel sulfide deposits in Western Australia; II, Distribution within the ores and host
572 rocks at Kambalda. Economic Geology, 76(6), 1645-1674.

573 Kim, S.J., Lemaux, S., Demazeau, G., Kim, J.Y., and Choy, J.H. (2002) X-Ray absorption
574 spectroscopic study on $LaPdO_3$. Journal of Materials Chemistry, 12, 995–1000.

575 Kitakaze, A., Machida, T., and Komatsu, R. (2016) Phase relations in the Fe-Ni-S system
576 from 875 to 650°C. The Canadian Mineralogist, 54, 1175–1186.

577 Koningsberger, D.C., Mojet, B.L., van Dorssen, G.E., and Ramaker, D.E. (2000) XAFS
578 spectroscopy: Fundamental principles and data analysis. Topics in Catalysis, 10, 143-155.

579 Laurenz, V., Fonseca, R.O., Ballhaus, C., Jochum, K.P., Heuser, A., and Sylvester, P.J.
580 (2013) The solubility of palladium and ruthenium in picritic melts: 2. The effect of sulfur.
581 Geochimica et Cosmochimica Acta, 108, 172-183.

582 Lesher, C.M., and Keays, R.R. (2002) Komatiite-associated Ni–Cu–(PGE) deposits:
583 geology, mineralogy, geochemistry and genesis. Canadian Institute of Mining, Metallurgy and
584 Petroleum, 54, 579-618.

585 Li, C., and Ripley, E.M. (2006) Formation of Pt-Fe alloy by desulfurization of Pt-Pd
586 sulfide in the J-M reef of the Stillwater Complex, Montana. The Canadian Mineralogist, 44, 895–
587 903.

588 Liang, Q.L., Song, X.Y., Wirth, R., Chen, L.M., Yu, S.Y., Krivolutskaya, N. A., and Dai,
589 Z.H. (2022) Thermodynamic conditions control the valences state of semimetals thus affecting
590 the behavior of PGE in magmatic sulfide liquids. Geochimica et Cosmochimica Acta, 321, 1-15.

591 Liu, Y., and Brenan, J. (2015) Partitioning of platinum-group elements (PGE) and
592 chalcogens (Se, Te, As, Sb, Bi) between monosulfide-solid solution (Mss), intermediate solid
593 solution (Iss) and sulfide liquid at controlled fO_2 – fS_2 conditions. Geochimica et Cosmochimica
594 Acta, 159, 139-161.

595 Majzlan, J., Makovicky, M., Makovicky, E., and Rose-Hansen, J. (2002) The System Fe
596 Pt S at 1100 C. The Canadian Mineralogist. 40, 509–517.

597 Makovicky E., and Karup-Møller S. (2016) The Pd–Ni–Fe–S phase system at 550 and
598 400° C. The Canadian Mineralogist, 54(2), 377-400.

599 Makovicky, M., Makovicky, E., and Rose-Hansen, J. (1986) Experimental studies on the
600 solubility and distribution of platinum group elements in base-metal sulphides in platinum
601 deposits. In Conference metallogeny of basic and ultrabasic rocks (pp. 415-425).

602 Manceau, A., Merkulova, M., Murdzek, M., Batanova, V., Baran, R., Glatzel, P., Saikia,
603 B.K., Paktunc, D., and Lefticariu, L. (2018) Chemical forms of mercury in pyrite: implications

for predicting mercury releases in acid mine drainage settings. Environmental science and technology, 52(18), 10286-10296.

Manceau, A., Merkulova, M., Mathon, O., Glatzel, P., Murdzek, M., Batanova, V., Simionovici, A., Steinmann, S.N., and Paktunc, D. (2020) The Mode of Incorporation of As(-I) and Se(-I) in Natural Pyrite Revisited. ACS Earth and Space Chemistry, 4, 3, 379-390.

Mandziuk, Z.L., and Scott, S.D. (1977) Synthesis, stability, and phase relations of argentian pentlandite in the system Ag-Fe-Ni-S. The Canadian Mineralogist, 15(3), 349-364.

Mansur, E.T., Barnes, S.J., and Duran, C.J. (2019) Textural and compositional evidence for the formation of pentlandite via peritectic reaction: Implications for the distribution of highly siderophile elements. Geology, 47, 1-7.

Matkovic, P., El Boragy, M., and Schubert, K. (1976) Kristallstruktur von $Pd_{16}S_7$. Journal of Less-Common Metals, 50, 165-176 (In German).

Merkulova, M., Mathon, O., Glatzel, P., Rovezzi, M., Batanova, V., Marion, P., Boiron, M.-C., and Manceau, A. (2019) Revealing the Chemical Form of “Invisible” Gold in Natural Arsenian Pyrite and Arsenopyrite with High Energy-Resolution X-ray Absorption Spectroscopy. ACS Earth and Space Chemistry, 3, 1905–1914.

Mihalik, P., Hiemstra, S.A., and de Villiers, J.P.R. (1975) Rustenburgite and atokite, two new platinum-group minerals from the Merensky Reef, Bushveld igneous complex. The Canadian Mineralogist, 13, 146-150.

Muller, J.E., Jepsen, O., and Wilkins, J.W. (1982) X-ray absorption spectra: K-edges of 3d transition metals, L-edges of 3d and 4d metals, and M-edges of palladium. Solid state communications, 42, 365-368.

Naldrett, A.J. (2011) Fundamentals of magmatic sulfide deposits. Reviews in Economic Geology. 17, 1–50.

Pagé, P., and Barnes, S. J. (2016) The influence of chromite on osmium, iridium, ruthenium and rhodium distribution during early magmatic processes. Chemical Geology, 420, 51-68.

Pokrovski, G.S., Kokh, M.A., Proux, O., Hazemann, J.L., Bazarkina, E.F., Testemale, D., Escoda, C., Boiron, M.C., Blanchard, M., Aigouy, T., Gouy, S., de Parseval, P., and Thibaut, M. (2019) The nature and partitioning of invisible gold in the pyrite-fluid system. Ore Geology Reviews, 109, 545-563.

Rajamani, V. and Prewitt, C.T. (1975) Thermal expansion of the pentlandite structure. American Mineralogist, 60, 39-48.

Ravel, B., and Newville, M. (2005) ATHENA, ARTEMIS, HEPHAESTUS: data analysis for X-ray absorption spectroscopy using IFEFFIT. Journal of Synchrotron Radiation, 12, 537-541.

Riley, J.F. (1977) The pentlandite group (Fe, Ni, Co)$_9$S$_8$: New data and an appraisal of structure-composition relationships. Mineralogical Magazine, 41(319), 345-349.

Sham, T.K. (1985) L-edge x-ray-absorption systematics of the noble metals Rh, Pd, and Ag and the main-group metals In and Sn: A study of the unoccupied density of states in 4d elements. Physical Review B, 31, 1888–1902.

Shannon, R.D. (1976) Revised Effective ionic radii and systematic studies of interatomic distances in halides and chalcogenides. Acta Crystallographica, 32, 751-767.

Shishkin, N.N. (1972) Silver-rich variety of pentlandite. International Geology Review, 14(5), 505-511.

Sittner, J., Brovchenko, V., Siddique, A., Buyse, F., Boone, M., Renno, A.D., Cnudde, V., Merkulova, M., and Sluzhenikin, S.F. (2022) Three-Dimensional Distribution of Platinum Group Minerals in Natural MSS-ISS Ores From the Norilsk One Deposit, Russia. Frontiers in Earth Science.

Sluzhenikin, S.F., Yudovskaya, M.A., Barnes, S.J., Abramova, V.D., Le Vaillant, M., Petrenko, D.B., Grigor'eva, A.V., and Brovchenko, V.D. (2020) Low-Sulfide Platinum Group Element Ores of the Norilsk-Talnakh Camp. Economic Geology 115(6), 1267-1303.

Solé, V.A., Papillon, E., Cotte, M., Walter, P., and Susini, J. (2007) A multiplatform code for the analysis of energy-dispersive X-ray fluorescence spectra. Spectrochimica Acta - Part B Atomic Spectroscopy, 62, 63–68.

Tagirov, B.R., Trigub, A.L., Kvashnina, K.O., Shiryaev, A.A., Chareev, D.A., Nickolsky, M.S., Abramova, V.D., and Kovalchuk, E.V. (2016) Covellite CuS as a matrix for "invisible" gold: X-ray spectroscopic study of the chemical state of Cu and Au in synthetic minerals. Geochemica et Cosmochimica Acta, 191, 58-69.

Todorovic, R. (2012) Understanding XANES of Supported Pd Particles: Size, Adsorbate and Alloy Effects, 49 p, Master Thesis, University of Illinois, Chicago.

Tredoux, M., Davies, G., McDonald, I., and Lindsay, N.M. (1995) The fractionation of platinum-group elements in magmatic systems, with the suggestion of a novel causal mechanism. South African Journal of Geology, 98(2), 157-167.

668 Trigub, A.L., Tagirov, B.R., Kvashnina, K.O., Chareev, D.A., Nickolsky, M.S., Shiryaev,
669 A.A., Baranova, N.N., Kovalchuk, E.V., and Mokhov, A.V. (2017) X-ray spectroscopy study of
670 the chemical state of "invisible" Au in synthetic minerals in the Fe-As-S system. American
671 Mineralogist, 102, 1057-1065.

672 Vaasjoki, O., Hakli, T. A., and Tontti, M. (1974) The effect of cobalt on the thermal
673 stability of pentlandite. Economic Geology, 69(4), 549-551.

674 Wirth, R., Reid, D., and Schreiber, A. (2013) Nanometer-sized platinum-group minerals
675 (PGM) in base metal sulfides: New evidence for an orthomagmatic origin of the Merensky reef
676 PGE ore deposit, Bushveld Complex, South Africa. The Canadian Mineralogist, 51, 143-155.

677 Witjens, L.C., Bitter, J.H., Van Dillen, A.J., De Jong, K.P., and De Groot, F.M.F. (2004)
678 Pd L_3 edge XANES investigation of the electronic and geometric structure of Pd/Ag-H
679 membranes. Physical Chemistry Chemical Physics, 6, 3903–3906.

680 Zheng, L., Zhao, Y.D., Tang, K., Ma, C.Y., Han, Y., and Cui, M.Q. (2011) Total electron
681 yield mode for XANES measurements in the energy region of 2.1- 6.0 keV. Chinese Physics C,
682 35, 199–202.

683

684 **Figure legends**

685 **Figure 1.** (**a**) Micro-XRF map of pentlandite (Pn) and two PGM grains (PGM_1 and PGM_2) RM
686 30_3_9b. Map size: 170×69 μm^2, pixel size: 3 μm; (**b**) μXRF map of PGM_3 grain RM 10_3_10a.
687 Map size: 20×20 μm^2, pixel size: 2 μm. Pd – red, Ni – green, Cu – blue.

688 **Figure 2.** (**a**) Micro-XRF spectra of four Pd "hot" spots in different pentlandite (Pn) grains.
689 Micro-XRF spectra for areas RM 29_1_8a, RM 29_3_7a, and RM 30_3_9b were collected with
690 3174 eV incident beam and 300 s collection time. μXRF spectrum for the area RM 29_1_1a was
691 obtained by summing 192 Pd-rich pixels of the μXRF map RM 29_1_1a recorded at 3174 eV
692 with 1 s per point; (**b**) Micro-XRF spectra of Pd-rich pentlandite in the area RM 30_3_9b, PGM
693 grain in the area RM 10_3_10a, Pd-poor pentlandite (matrix Pn) and ISS (matrix ISS). Micro-
694 XRF spectra for areas with Pd-rich pentlandite and PGM were obtained with 3174 eV incident
695 beam and 300 s collection time. μXRF spectra for Pn matrix and ISS matrix were obtained by
696 summing 150 and 140 pixels respectively on the μXRF map of the area RM 29_1_ recorded at
697 3174 eV with 1 s per point.

698 **Figure 3.** (**a**) BSE photo of the contact pentlandite located between ISS globule and MSS with
699 the EPMA profile. The EPMA data from the profile are presented in apu on (**b, c**) – Ni vs Pd and
700 Fe vs Pd correspondingly.

701 **Figure 4.** EBSD data collected from heterogeneous Pd-rich pentlandite grain, (**a**) and (**b**)
702 correspondingly - EBSD patterns collected from Pd-rich and Pd-free areas; (**c**) - EDX mapping of
703 the corresponding grain in Ni and Pd characteristic X-rays; (**d**) - diffraction quality map; (**e**) -
704 Euler-colored orientation map and corresponding inverse pole figure, (**f**) - local misorientation
705 map depicting local strains and deformations and local disorientation graph; (**g**) - map of

706 disorientation from average depicting grain modularity and disorientation directions and
707 corresponding coloring legend.

708 **Figure 5.** Pd L_3-edge XANES spectra for Pd-rich pentlandite from the area RM 30_3_9b (Pn),
709 PGM from the area RM 10_3_10a (PGM) compared to the spectra of PGM grains (**a**), and Pd
710 references (**b**). The white line is indicated as *a'*, the second spectral feature is indicated as *b'*.

711

This is the peer-reviewed, final accepted version for American Mineralogist, published by the Mineralogical Society of America.
The published version is subject to change. Cite as Authors (Year) Title. American Mineralogist, in press.
DOI: https://doi.org/10.2138/am-2022-8704. http://www.minsocam.org/

712 **Table 1.** List of investigated samples.

Name	Sample/ inventory number	General formula	Origin	Geological setting	[Pd] wt%
Pentlandite and PGM	RM 10, RM 29, RM 30	$(Fe,Ni)_9S_8$ pentlandite	Mt. Rudnaya, Norilsk, Russia	magmatic	up to 4.84[a,c] pentlandite
Atokite	75793	$Pd_{2.25}Pt_{0.75}Sn$	Oktyabrsky mine, Norilsk, Russia	magmatic	47.47[b]
Cabriite	80761	Pd_2CuSn	Oktyabrsky mine, Norilsk, Russia	magmatic	46.19[c]
Paolovite	80761	Pd_2Sn	Oktyabrsky mine, Norilsk, Russia	magmatic	64.20[b]
Sobolevskite	80762	Pd(Bi,Te)	Oktyabrsky mine, Norilsk, Russia	magmatic	31.31[c]
Vasilite	80272	$Pd_{15.93}Pt_{0.18}Cu_{0.21}S_{6.68}$	Miass river, Ural, Russia	alluvial	87.9[c]
Majakite	75810	PdNiAs	Oktyabrsky mine, Norilsk, Russia	magmatic	44.34[b]

[a] *concentration based on LA-ICP-MS analyses*
[b] *concentration based on empirical mineral formula*
[c] *concentration based on EPMA analysis*

713

714

715 **Table 2**. White line (WL) energy positions for Pd L_3-edge XANES spectra. pn – pentlandite.

Sample	WL position, eV
Pd foil	3173.8
$PdCl_2$	3174.41
PdS	3175.3
$PdSO_4$	3174.7
atokite	3175
cabriite	3175.3
paolovite	3175.6
sobolevskite	3175.3
vasilite	3174.7
majakite	3175.3
pn in RM 30_3_9b	3174.7
pn in RM 29_1_8a	3174.69
pn in RM 29_3_7a	3174.69
pn in RM 29_1_1a	3174.7
PGM in RM 10_3_10a	3175.1

716

717

This is the peer-reviewed, final accepted version for American Mineralogist, published by the Mineralogical Society of America.
The published version is subject to change. Cite as Authors (Year) Title. American Mineralogist, in press.
DOI: https://doi.org/10.2138/am-2022-8704. http://www.minsocam.org/

718 **Figure 1**

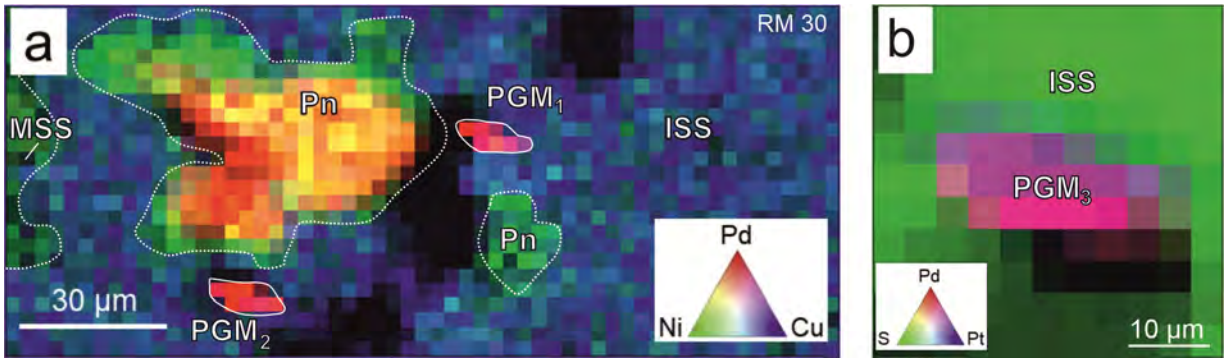

719

720

This is the peer-reviewed, final accepted version for American Mineralogist, published by the Mineralogical Society of America.
The published version is subject to change. Cite as Authors (Year) Title. American Mineralogist, in press.
DOI: https://doi.org/10.2138/am-2022-8704. http://www.minsocam.org/

721 **Figure 2**

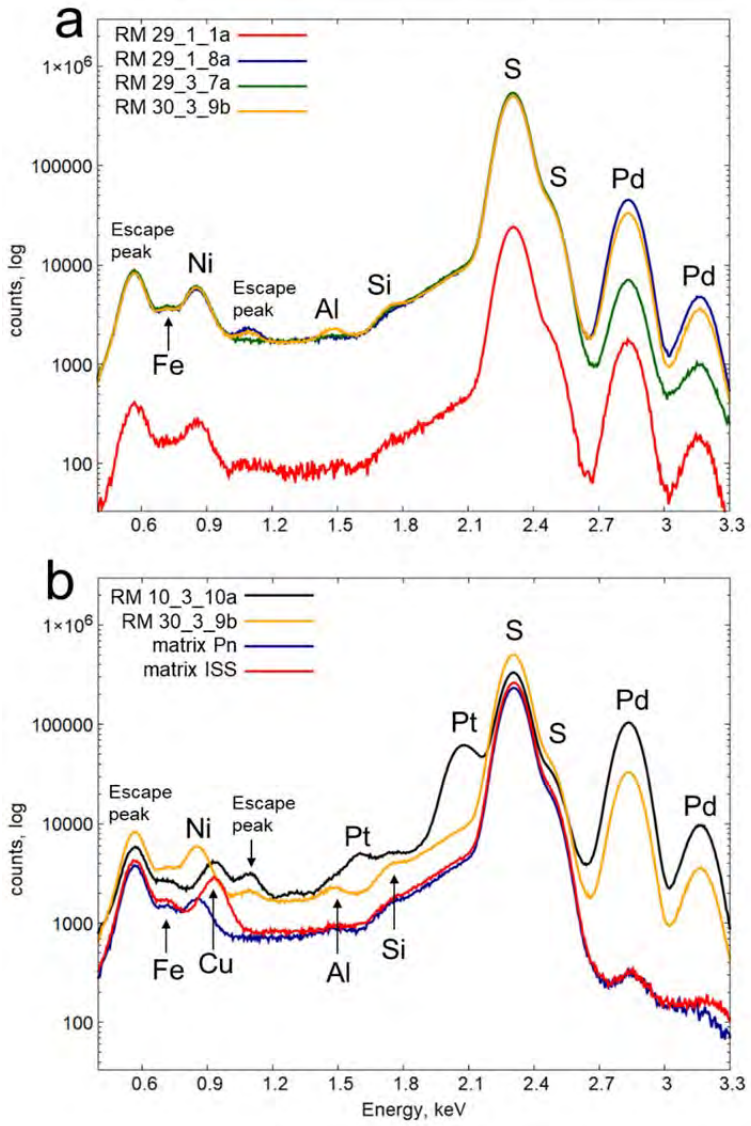

722

723

This is the peer-reviewed, final accepted version for American Mineralogist, published by the Mineralogical Society of America.
The published version is subject to change. Cite as Authors (Year) Title. American Mineralogist, in press.
DOI: https://doi.org/10.2138/am-2022-8704. http://www.minsocam.org/

724 **Figure 3**

725

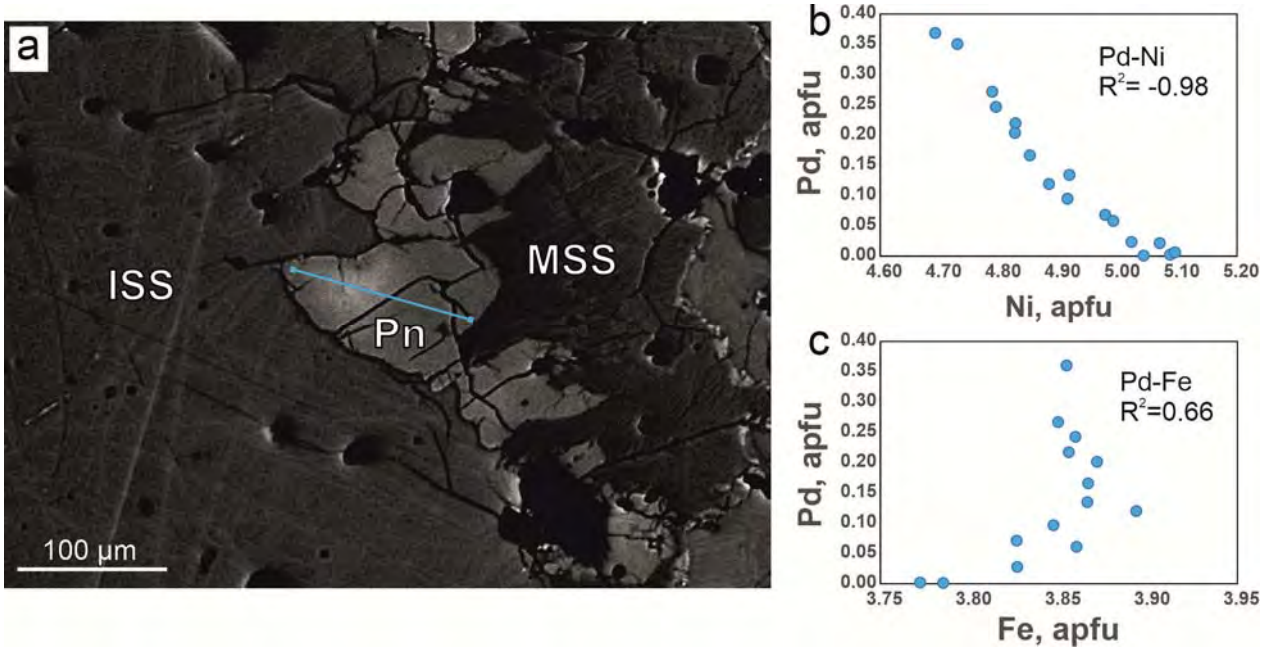

726

727

This is the peer-reviewed, final accepted version for American Mineralogist, published by the Mineralogical Society of America.
The published version is subject to change. Cite as Authors (Year) Title. American Mineralogist, in press.
DOI: https://doi.org/10.2138/am-2022-8704. http://www.minsocam.org/

728 **Figure 4**

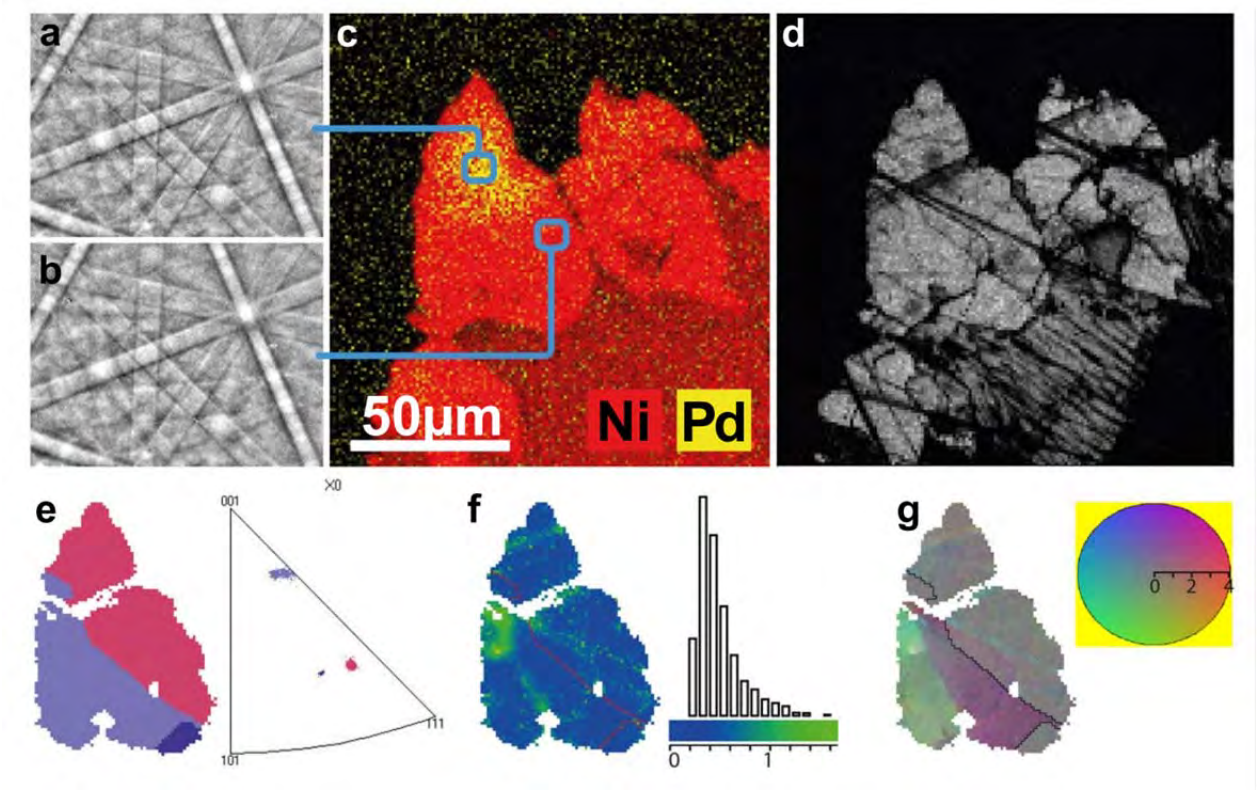

729

730

This is the peer-reviewed, final accepted version for American Mineralogist, published by the Mineralogical Society of America.
The published version is subject to change. Cite as Authors (Year) Title. American Mineralogist, in press.
DOI: https://doi.org/10.2138/am-2022-8704. http://www.minsocam.org/

731 **Figure 5**

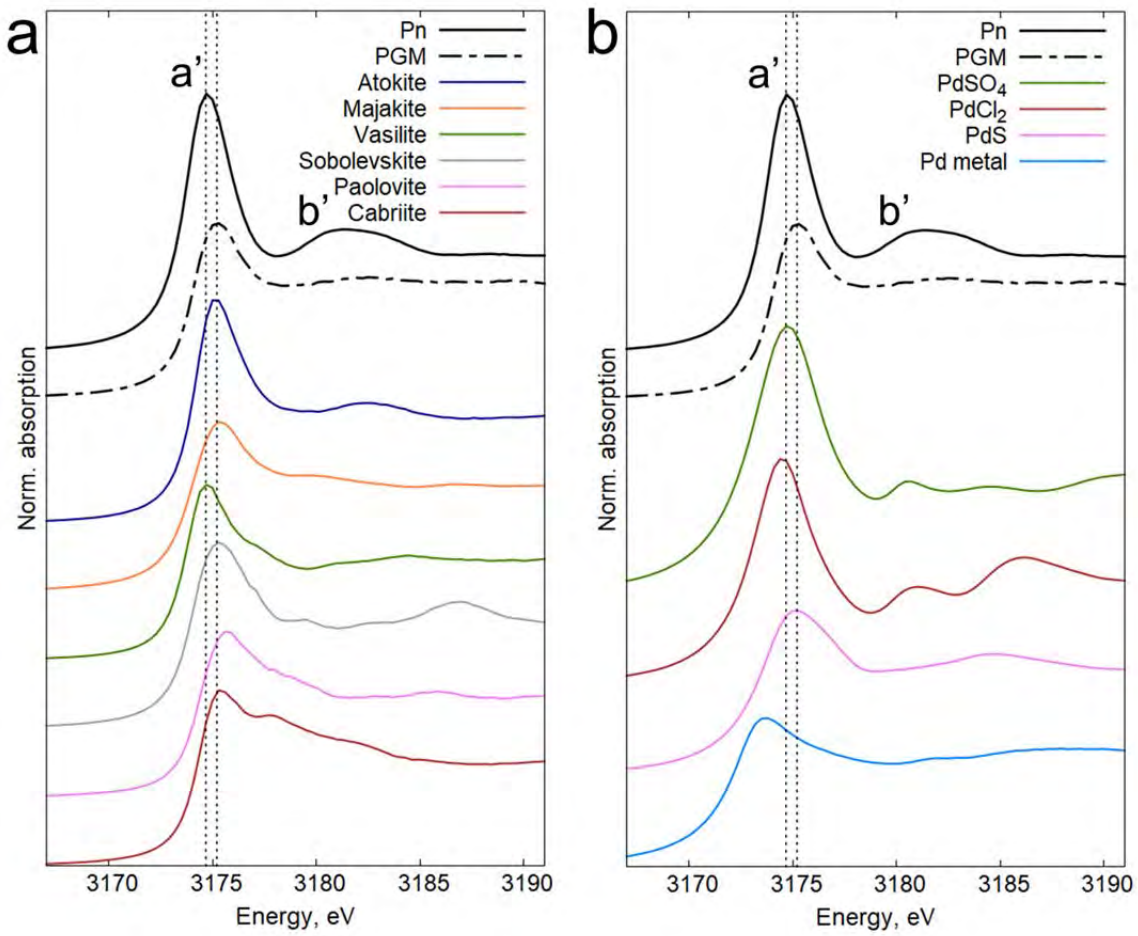

732

733